Piezoaeroelastic Modeling and Analysis of a Generator Wing with Continuous and Segmented Electrodes

CARLOS DE MARQUI JR,[1,*] ALPER ERTURK[2] AND DANIEL J. INMAN[2]

[1]*Department of Aeronautical Engineering, Engineering School of Sao Carlos, University of Sao Paulo, Brazil*

[2]*Department of Mechanical Engineering, Center for Intelligent Material Systems and Structures, Virginia Tech, USA*

ABSTRACT: Unmanned air vehicles (UAVs) and micro air vehicles (MAVs) constitute unique application platforms for vibration-based energy harvesting. Generating usable electrical energy during their mission has the important practical value of providing an additional energy source to run small electronic components. Electrical energy can be harvested from aeroelastic vibrations of lifting surfaces of UAVs and MAVs as they tend to have relatively flexible wings compared to their larger counterparts. In this work, an electromechanically coupled finite element model is combined with an unsteady aerodynamic model to develop a piezoaeroelastic model for airflow excitation of cantilevered plates representing wing-like structures. The electrical power output and the displacement of the wing tip are investigated for several airflow speeds and two different electrode configurations (continuous and segmented). Cancelation of electrical output occurs for typical coupled bending-torsion aeroelastic modes of a cantilevered generator wing when continuous electrodes are used. Torsional motions of the coupled modes become relatively significant when segmented electrodes are used, improving the broadband performance and altering the flutter speed. Although the focus is placed on the electrical power that can be harvested for a given airflow speed, shunt damping effect of piezoelectric power generation is also investigated for both electrode configurations.

Key Words: energy harvesting, piezoaeroelasticity, piezoceramics, aeroelasticity, electrode configuration, unmanned air vehicles.

INTRODUCTION

MULTIFUNCTIONAL structures are pointed out as a future breakthrough technology for micro air vehicles (MAVs) and unmanned air vehicles (UAVs) design (Pines and Bohorquez, 2006). An additional task to the primary load-bearing function of these aircraft structures is to provide an additional source of electrical energy by converting the vibrations available in their environment to electricity through the concept of vibration energy harvesting (Sodano et al., 2004; Beeby et al., 2006; Anton and Sodano, 2007; Priya, 2007; Cook-Chennault et al., 2008). A possible source of energy for UAVs and MAVs is the mechanical vibration energy due to unsteady aerodynamic loads during the flight (Anton and Inman, 2008) or due to ground excitation in perching (Magoteaux et al., 2008; Erturk et al., 2009a). Although other transduction mechanisms exist, piezoelectric transduction has received the most attention for vibration-based energy harvesting and several review articles have appeared in the last 4 years (Sodano et al., 2004; Beeby et al., 2006; Anton and Sodano, 2007; Priya, 2007; Cook-Chennault et al., 2008).

Piezoelectric power generators can harvest electrical energy from mechanical vibrations based on the direct piezoelectric effect. Researchers have proposed various models to represent the electromechanical behavior of piezoelectric energy harvesters over the last 5 years (Erturk and Inman, 2008a). More recently, analytical distributed parameter solutions for unimorph and bimorph piezoelectric energy harvester configurations with closed-form expressions have been presented (Erturk and Inman, 2008b, 2009). Electromechanically coupled finite element (FE) formulation (De Marqui et al., 2009a; Elvin and Elvin, 2009; Rupp et al., 2009; Yang and Tang, 2009) is another way of modeling the dynamics of piezoelectric energy harvesters. An electromechanically coupled FE model (De Marqui et al., 2009a) has been successfully verified against the analytical results obtained from the closed-form solution for a unimorph harvester under base excitation (Erturk and Inman, 2008b) and also against the analytical and experimental results for a bimorph energy harvester with a tip mass under base excitation (Erturk and Inman, 2009). The FE model has also been used to solve an optimization problem for UAV applications. The aluminum wing

*Author to whom correspondence should be addressed.
E-mail: demarqui@sc.usp.br
Figures 1, 2 and 4–10 appear in color online: http://jim.sagepub.com

1045-389X/10/10 0983–11 $10.00/0 DOI: 10.1177/1045389X10372261

spar of a UAV is modified to design a generator wing spar. Since mass densities of typical piezoceramics are considerably large for UAV applications, a limiting value for mass addition is imposed to the problem as a design constraint. Dimensions of the embedded piezoceramic are identified for the maximum electrical power output of the generator spar with embedded piezoceramics (De Marqui et al., 2009a).

Cantilevered piezoelectric energy harvesters are thin structures with one or more piezoceramic layers excited mainly due to the motion of their base. Usually, conductive electrode pairs cover the surfaces of the piezoceramic layers continuously. The electric charge collected by these electrodes is a function of the electric displacement in the piezoceramic during vibrations and the electric displacement is function of the dynamic strain distribution throughout the length of the harvester. Therefore cancelation of electrical output occurs for modes of a cantilevered harvester other than the fundamental one when continuous electrodes are used. If the electrodes are discontinuous at the strain nodes (where dynamic strain distribution changes sign for a vibration mode) cancellation of the electrical output can be avoided with the proper combination of the out-of-phase voltages of each segment (Erturk et al., 2009b). However, typical piezoelectric energy harvesters are symmetric structures and torsional modes are not excited in the base excitation problem. It is possible to conclude that the electrical energy is always extracted from the bending modes for symmetric cantilevers in the base excitation problem. Even when an asymmetric tip mass is considered (De Marqui et al., 2009b) (which excites the torsional modes) using continuous electrodes results in cancellation of the potential of electrical energy that can be extracted from the torsion-dominated vibration mode(s) and the significant electrical energy is harvested from the bending-dominated vibration mode(s) only.

The literature of piezoaeroelasticity or active aeroelasticity includes the use of smart materials (piezoelectric materials are of particular interest in this work) as sensors or actuators. Most of the existing research use piezoceramics and piezo-fiber-composites as actuators to modify the aeroelastic response or to suppress aeroelastic instabilities (Lazarus et al., 1995; McGowan et al., 1996; Friedmann, 1998; Librescu and Na, 2000; Cesnik and Ortega-Morales, 2001; Cesnik and Shin, 2001; Brown, 2003). Macro-fiber-composite (MFC) actuators are used to suppress buffeting vibrations on the vertical fins of an F-18 (Sheta et al., 2003; Wickramasinghe et al., 2007). Researchers have also used piezoelectric materials as actuators for morphing wings or morphing aircraft (Schultz and Hyer, 2004; Bilgen et al., 2007). Piezoelectric materials can also be associated with external passive circuits (resistors or resonant circuits) to increase the passive damping of aeroelastic systems (Agneni et al., 2003, 2006). Agneni et al. (2003, 2006) observed a weak capability of improving the flutter margin of a wing, but a good performance in reducing gust response of a commercial glider at airspeeds close to flutter. Anton and Inman (Anton and Inman, 2008) presented an experimental study on electrical power generation from the structural vibrations of a radio controlled glider in flight using piezoelectric patches at the roots of the wings and a piezoelectric cantilever inside the fuselage. Although aeroelastic vibrations constitute a useful additional energy source for UAVs and MAVs, piezoaeroelastic modeling of the concept of a *power generator wing* has not been covered in the literature.

In this article, the use of continuous and segmented electrodes is investigated for energy harvesting from aeroelastic vibrations of a cantilevered plate representing a wing-like structure. The piezoaeroelastic model is obtained by combining an unsteady vortex-lattice model (VLM) (Katz and Plotkin, 2001; Benini et al., 2004) and an electromechanically coupled FE model previously presented by the authors (De Marqui et al., 2009a). The electrical power output and the displacement at the wing tip are investigated for several airflow speeds using the continuous- and segmented-electrode configurations. Cancelation of electrical output occurs for coupled bending-torsion aeroelastic modes of a cantilevered generator wing when continuous electrodes are used. Torsional motions of the coupled aeroelastic modes become significant when the electrodes are discontinuous at a certain position of the piezoceramics (a straight line from the root to the tip), improving broadband or varying-frequency excitation performance of the generator wing. A multi-segment electrode configuration with proper combination of the out-of-phase electrical outputs for the practical modes of interest would provide improved broadband energy harvesting performance. Although the main goal here is to estimate the electrical power output for each airflow speed (both for the continuous- and the segmented-electrode cases), the effect of piezoelectric shunt damping on the aeroelastic response of the generator wing is also investigated. As a consequence of the improved electromechanical coupling with segmented electrodes, an improved shunt damping effect is observed for the aeroelastic behavior since the piezoelectric reaction of the torsional mode is improved with the segmented-electrode configuration.

A PIEZOAEROELASTIC FINITE ELEMENT MODEL

Cantilever Piezoelastic Plate with Continuous and Segmented Electrodes

The piezoaeroelastic model is obtained by combining an electromechanically coupled FE model (De Marqui et al., 2009a) and an unsteady VLM (Katz and Plotkin,

2001; Benini et al., 2004). The electromechanically coupled FE model is based on the Kirchhoff assumptions to model the thin cantilevered wing with embedded piezoceramic layers shown in Figure 1. The substructure and the piezoceramic layers are assumed to be perfectly bonded to each other. The piezoceramic layers (which are poled in the thickness direction) are covered by continuous electrodes (which are assumed to be perfectly conductive) of negligible thickness. A resistive electrical load is considered and the purpose is to estimate the power generated in the electrical domain due to the aeroelastic vibrations of the energy harvester wing. A rectangular finite element with four nodes and three mechanical degrees of freedom per node is used to model the substructure. An electrical degree of freedom is added to the finite element to model the piezoceramic layers (13 degrees of freedom in total). A transformation is imposed in the formulation in order to account for the presence of conductive electrodes bracketing each piezoceramic layer. This way a single electrical output and a single capacitance are defined for each electrode pair (De Marqui et al., 2009a).

The governing piezoaeroelastic equations for the generator wing are:

$$\mathbf{M}\ddot{\boldsymbol{\Psi}} + \mathbf{C}\dot{\boldsymbol{\Psi}} + \mathbf{K}\boldsymbol{\Psi} - \tilde{\boldsymbol{\Theta}} v_p = \mathbf{F}, \tag{1}$$

$$C_p \dot{v}_p + \frac{v_p}{R_l} + \tilde{\boldsymbol{\Theta}}^t \dot{\boldsymbol{\Psi}} = 0, \tag{2}$$

where $\mathbf{M}$ is the global mass matrix, $\mathbf{K}$ is the global stiffness matrix, $\mathbf{C}$ is the global damping matrix (assumed here as proportional to the mass and stiffness matrices), $\tilde{\boldsymbol{\Theta}}$ is the effective electromechanical coupling vector, $\boldsymbol{\Psi}$ is the vector of mechanical coordinates (nodal mechanical variables), C_p is the effective capacitance of the piezoceramic, R_l is the load resistance, v_p is the voltage across the load and the superscript t stand for transpose (De Marqui et al., 2009a). The right-hand-side term $\mathbf{F}$ in Equation (1) represents the unsteady aerodynamic loads obtained using the unsteady VLM.

The bimorph cross-section shown in Figure 1 allows combining the electrical outputs of the upper (A) and the lower (B) piezoceramic layers either in series or in parallel. For instance, if the layers are oppositely poled in the thickness direction as depicted in Figure 1, connection of the bottom electrode of layer A with the top electrode of layer B is the series connection case (the remaining two electrodes are connected to the load). For this configuration, the effective electromechanical coupling vector is equal to that of one piezoceramic layer and the effective capacitance is one half of the capacitance of one piezoceramic layer.

For a torsional vibration mode with the nodal line corresponding to the center line of the width, strong cancellations occur in both layers (A and B) of the configuration shown in Figure 1. The segmented-electrode configuration shown in Figure 2 is proposed to avoid this cancellation. When the four electrodes are segmented to give eight electrodes as depicted in Figure 2, one has several options for combining the electrical outputs of these four regions. To avoid cancellation of the electrical output of the fundamental torsional mode, the alternative considered in this case study is to combine the resulting electrical outputs of the upper (A1 and A2) and lower (B1 and B2) piezoceramics in series. Parallel connection of A1 and A2 can be combined with the parallel connection of B1 and B2 as follows: the bottom electrode of A1, the top electrode of A2, the top electrode of B1 and the bottom electrode of B2 are connected. The top electrode of A1 and the bottom electrode of A2 are connected to one terminal of the electrical load whereas the bottom electrode of B1 and the top electrode of B2 are connected to its opposite terminal. In the discussion given

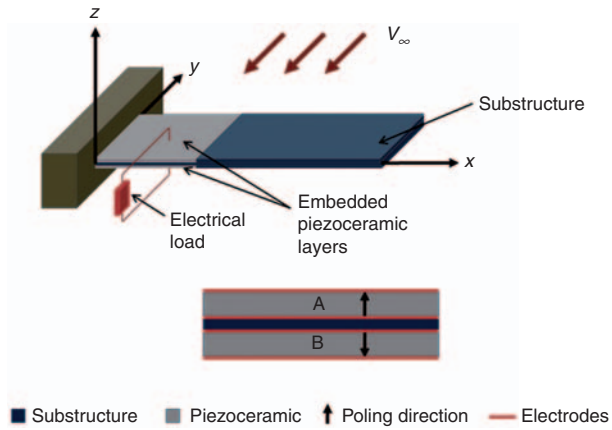

Figure 1. *A piezoelectric power generator wing under flow excitation and the cross-sectional view of the region with embedded piezoceramics and continuous electrodes.*

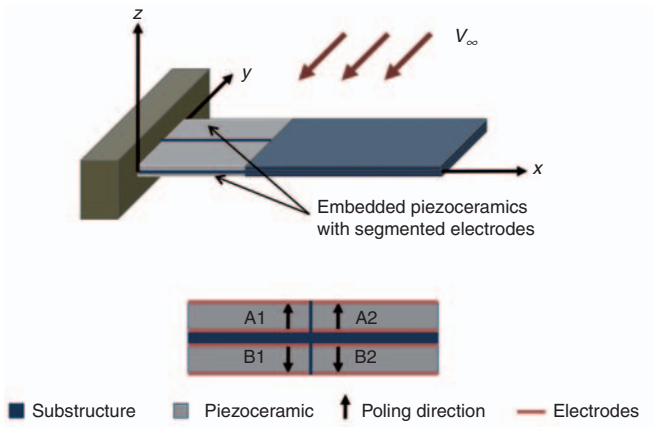

Figure 2. *A piezoelectric power generator wing under flow excitation and the cross-sectional view of the region with embedded piezoceramics and segmented electrodes.*

here, it is assumed that the substructure material does not provide conductivity between the electrodes. In practice, epoxy or Kapton layers can be employed for this purpose.

Note that, as experimentally shown by Kim et al. (2005a,b) for energy harvesting from static deflection of a circular plate, one can change the polarization of the segments and use continuous electrodes. However, as discussed by Erturk et al. (2009b), Rupp et al. (2009), in the dynamic (vibration) problem, using segmented electrodes is more convenient to avoid cancellations in different vibration modes. In addition, combining the segmented electrodes as mentioned above will cause cancellation of the electrical outputs in the bending modes. In practice, one might need to use diodes to avoid such cancellations (Erturk et al., 2009b). In the segmented-electrode simulations given here, the combination of the electrodes for each mode is assumed to be such that there is no cancellation. For this purpose, the sign of the effective piezoelectric constant is defined to be mode shape dependent (the same sign for the bending modes and changes sign at the segment lines for the torsional modes). It is important to mention that, in the segmented solution given here, the effective capacitance and the electromechanical coupling vector are the same as the bimorph in series with continuous electrodes previously described (except for the signs of the elements of the electromechanical coupling vector are defined to be mode shape dependent).

Unsteady Aerodynamic Model

An unsteady VLM is used to obtain the loads over a cantilever plate-like wing (Katz and Plotkin, 2001; Benini et al., 2004). The wing is represented as a thin lifting surface and it is divided into a number of elements (panels). A planar vortex ring is associated with each rectangular panel of the body itself and its wake. The vortex singularity is a solution for the Laplace equation and the aerodynamic loads on the wing can be obtained by combining these singularities with the incompressible potential flow around the body.

A typical vortex-lattice mesh for the three-dimensional flow problem is shown in Figure 3. The leading segment of each vortex ring is placed at the quarter chord point of each panel and a control point is placed at the three-quarter chord of each panel, where the boundary condition is verified. If the surface of the plate-like wing has m panels ($m = R \times S$, where R and S are the number of panels along the chord and the span, respectively) and consequently m vortex rings and control points, one can express the boundary condition as:

$$\mathbf{a}_{KL}\boldsymbol{\Gamma}_{m,1} = \left[\mathbf{v}_{m_{m,1}} + \mathbf{v}_{w_{m,1}}\right] \cdot \mathbf{n}_{m,1}, \tag{3}$$

where $\mathbf{a}_{KL}$ is the influence coefficient that relates the circulation at the vortex ring K to the inner product of the perturbed velocity at point L. Both counters K and L can have values from 1 to $R \times S$. For example to scan all the vortex rings influencing the control point K, an inner scanning loop is need with the counter $L = 1 \rightarrow S \times R$. The unknowns in this linear set of equations are the circulations $\boldsymbol{\Gamma}_m$ of each vortex ring. The term $\mathbf{v}_m$ is always known at each time step as it depends on the free stream velocity and the velocities of the control points due to structural deformations. The velocities induced by the wake $\mathbf{v}_w$ are also known at each time step. New vortex rings are formed and shed from the trailing edge to the wake at each time step and the Kutta condition is satisfied imposing the circulation values of the most recently shed vortex rings are the same as those at the trailing edge (shedding vortices) in the previous time step. The circulation values for the vortex rings placed on the wing are obtained from the solution of the linear system given by Equation (3). The aerodynamic load for each panel can then be calculated from the unsteady Bernoulli equation (Katz and Plotkin, 2001; Benini et al., 2004).

Combination of the Models and the Numerical Integration Scheme

The equations of motion obtained from the FE formulation can be represented in modal domain as:

$$\bar{\mathbf{M}}\ddot{\boldsymbol{\eta}} + \bar{\mathbf{C}}\dot{\boldsymbol{\eta}} + \bar{\mathbf{K}}\boldsymbol{\eta} - \boldsymbol{\Phi}^{t}\tilde{\boldsymbol{\Theta}}v_p = \boldsymbol{\Phi}^{t}\mathbf{F}, \tag{4}$$

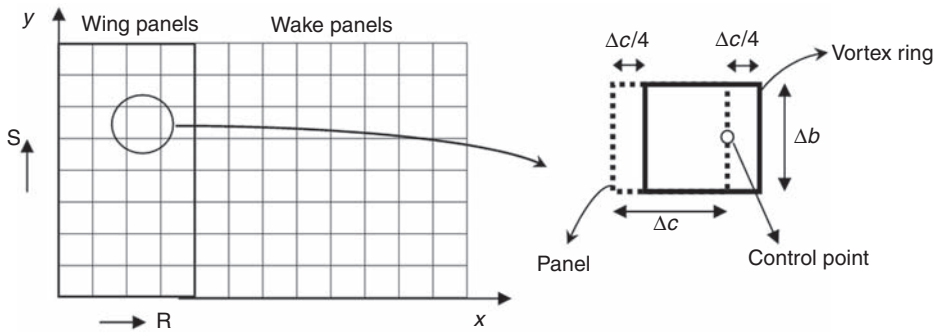

Figure 3. *Vortex-lattice mesh for a cantilevered wing.*

$$C_p\dot{v}_p + \frac{v_p}{R_l} + \tilde{\boldsymbol{\Theta}}^t\boldsymbol{\Phi}^t\dot{\boldsymbol{\eta}} = 0, \tag{5}$$

where $\boldsymbol{\eta}$ is the vector of modal coordinates, $\boldsymbol{\Phi}$ is the modal matrix (mass normalized so that the modal mass $\bar{\mathbf{M}}$ is the identity matrix), $\bar{\mathbf{C}}$ is the diagonal modal damping matrix, $\bar{\mathbf{K}}$ is the diagonal modal stiffness matrix and $\mathbf{F}$ is the vector of aerodynamic loads. This is the decoupled form (De Marqui et al., 2009a) of the equations of motion (in the modal sense), hence the solution can be expressed considering the most significant modes in the aeroelastic problem.

The solution of this piezoaeroelastic model in time domain has a particular complexity: the dependence between the electromechanical solution and the aerodynamic solution which are originally solved for distinct meshes (nodes of the FE mesh and control points of the VLM mesh). In order to obtain the aerodynamic loads one should know the structural response (and consequently the electrical response) which depends on the aerodynamic loads. An iterative method that accounts for the interaction between the aerodynamic and the electromechanical domains is used to solve the equations of motion. However, the aerodynamic loads and the structural motion are obtained from distinct numerical methods with distinct meshes. Therefore the structural FE nodes and the aerodynamic control points can be related as:

$$\boldsymbol{\Psi}_a = \mathbf{G}\boldsymbol{\Psi}, \tag{6}$$

where $\boldsymbol{\Psi}_a$ is the vector of mechanical coordinates of control points in the aerodynamic mesh, and $\mathbf{G}$ is the transformation matrix. The same transformation matrix can be used to write the structural mode shapes in terms of aerodynamic coordinates:

$$\boldsymbol{\Phi}_a = \mathbf{G}\boldsymbol{\Phi}, \tag{7}$$

where $\boldsymbol{\Phi}_a$ is the modal matrix in aerodynamic coordinates (corners of the vortex rings).

Since the virtual work done by the aerodynamic forces is the same for the representations in both domains, one can express:

$$\delta\boldsymbol{\Psi}_a^t\mathbf{F}_a = \delta\boldsymbol{\Psi}^t\mathbf{F}, \tag{8}$$

and $\mathbf{F}_a$ are the aerodynamic loads at the control points and $\mathbf{F}$ are the aerodynamic loads on the structural mesh (nodes). Using Equations (7) and (8), the equations of motion (Equations (4) and (5)) can be written as:

$$\bar{\mathbf{M}}\ddot{\boldsymbol{\eta}} + \bar{\mathbf{C}}\dot{\boldsymbol{\eta}} + \bar{\mathbf{K}}\boldsymbol{\eta} - \boldsymbol{\Phi}^t\tilde{\boldsymbol{\Theta}}v_p = \boldsymbol{\Phi}_a^t\mathbf{F}_a, \tag{9}$$

$$C_p\dot{v}_p + \frac{v_p}{R_l} + \tilde{\boldsymbol{\Theta}}^t\boldsymbol{\Phi}^t\dot{\boldsymbol{\eta}} = 0, \tag{10}$$

where the aerodynamic loads are transformed to the nodes of the structural mesh. In addition, the structural displacements obtained at the nodes of the FE mesh at each time step have to be obtained at the corners of vortex rings (in the aerodynamic mesh) for calculation of the aerodynamic loads. Hence, another transformation matrix is introduced to convert the modal coordinates to the corners of the vortex rings:

$$\mathbf{x}_a = \boldsymbol{\Phi}_a^*\boldsymbol{\eta}, \tag{10}$$

where $\mathbf{x}_a$ is the vector of aerodynamic coordinates and the matrices $\boldsymbol{\Phi}_a$ and $\boldsymbol{\Phi}_a^*$ are interpolated in this work using surface splines (Harder and Desmarais, 1972).

The equations of motion can be written as a system of $2n+1$ first order ordinary-differential equations, where n is the number of vibration modes taken into account in the solution. The vector of state variables can be given as:

$$\mathbf{y} = \begin{Bmatrix} \mathbf{y}_1 & \mathbf{y}_2 & y_3 \end{Bmatrix}^t, \tag{11}$$

where $\mathbf{y}_1 = \boldsymbol{\eta}$, $\mathbf{y}_2 = \dot{\boldsymbol{\eta}}$ and $y_3 = v_p$. Taking the derivative of $\mathbf{y}$ and using the mechanical and the electrical equations of motion (Equations (9) and (10)) one has $2n+1$ first-order ordinary differential equations:

$$\dot{\mathbf{y}}_1 = \mathbf{y}_2, \tag{12}$$

$$\dot{\mathbf{y}}_2 = \boldsymbol{\Phi}_a^t\mathbf{F}_a - \bar{\mathbf{C}}\mathbf{y}_2 - \bar{\mathbf{K}}\mathbf{y}_1 - \boldsymbol{\Phi}^t\tilde{\boldsymbol{\Theta}}\mathbf{y}_3, \tag{13}$$

$$\dot{y}_3 = \frac{1}{C_p}\left(-\tilde{\boldsymbol{\Theta}}^t\boldsymbol{\Phi}^t\mathbf{y}_2 - \frac{y_3}{R_l}\right). \tag{14}$$

The $2n+1$ ordinary differential equations with the aerodynamic loads applied at the FE nodes are then solved using a predictor-corrector scheme that accounts for the interaction between aerodynamic and electromechanical domains (Katz and Plotkin, 2001; Benini et al., 2004). The Adams-Bashforth-Moulton predictor-corrector method is used here and a detailed description of this method can be found in the literature (Lambert, 1991). The predictor uses the Adams-Bashforth method and the Adams-Moulton corrector. The local truncation error is given by Milne's estimate (Lambert, 1991) and a correction term can be included, which improves the accuracy of the result at each step.

CASE STUDY

This section presents case studies using the piezoaeroelastic model of a cantilevered plate-like wing with two identical layers of PZT-5A embedded into the top and the bottom of the aluminum structure. The piezoaeroelastic response of the generator wing is presented here as

time histories of the electrical power output and the wing tip displacement in the transverse direction. The input assumed in the simulations is a variation of three degrees in the flow direction for five time steps representing a sharp edge gust. The initial conditions are set to zero and the air density is assumed to be $1.225\,kg/m^3$.

Among the solutions obtained, we present results for three conditions: the first one at a low speed (hence low aerodynamic damping), the second one for an airflow speed around the maximum aerodynamic damping, and the third one at the flutter speed. Continuous electrodes covering the piezoceramic layers (poled in the opposite directions) are connected in series to a resistive electrical load (Figure 1) in these cases. For the flutter speed, the segmented electrode configuration depicted in Figure 2 is also investigated. In that case, the electrodes are segmented on the center line (mid-chord position) and properly combined to the resistive electrical load to avoid the cancelation of electrical output of the bending and the torsion modes (Figure 2). The piezoaeroelastic response characteristics of the continuous- and the segmented-electrode cases are then compared around the flutter speed for five different values of load resistance.

The material and the electromechanical properties of PZT-5A (www.efunda.com, 2009) are given in Table 1 and the plane-stress elastic, piezoelectric and dielectric terms to be used in the electromechanical FE model can be calculated with these data (De Marqui et al., 2009a).

The dimensions of the plate-like wing used in this work are $1200 \times 240 \times 3\ mm^3$. The identical piezoceramic layers have the same width as the wing chord. These embedded piezoceramics layers cover 30% of the wing span (at the root) and each one has a thickness of 0.5 mm. The geometric and material properties of the plate-like wing (aircraft aluminum alloy Al 2024-T3) are presented in Table 2 along with the constants of proportional damping for the overall structure.

The mode sequence and the undamped natural frequencies for the plate-like wing obtained from the FE model for short-circuit conditions (very low load resistance) are the first bending (1.68 Hz), the second bending (10.46 Hz), the first torsion (16.66 Hz), the third bending (27.74 Hz) and the second torsion (48.65 Hz), as given in Figure 4. The span-wise elastic axis and the center of gravity are coincident at 50% of chord.

The variation of total damping ratio (summation of structural damping and aerodynamic damping) for the second vibration mode (the mode that becomes unstable at flutter speed) with increasing airflow speed is presented in Figure 5. In the absence of airflow ($V = 0\,m/s$) and total damping is the available structural damping. The maximum aerodynamic damping is observed for airflow speeds around 30 m/s. As the airflow speed is further increased, the aerodynamic damping decreases and eventually vanishes at the flutter speed ($V = 40\,m/s$). It is important to note that damping has a major effect in vibration-based (aeroelastic vibrations in this case) power harvesting. Therefore larger mechanical amplitudes (and consequently larger electrical power outputs) are expected for large aerodynamic loads and low damping which is the case for airflow speeds around the flutter condition.

The piezoelectric power output extracted from the aeroelastic vibrations for an airflow speed of 10 m/s is shown in Figure 6(a). At this airflow speed, the total damping is slightly larger than the structural damping and the aerodynamic loads are not large (compared to higher speeds). As a consequence, the peak value of the power output is in the order of magnitude of 0.1 μW. One can observe in Figure 6(a) that power output increases as the load resistance is increased from $R_l = 10^2\,\Omega$ to $10^5\,\Omega$. As the load resistance is further increased to $R_l = 10^6\,\Omega$, the power output drops. Therefore, among the values of load resistance tested in this work, the maximum power output at this flow speed is observed for $R_l = 10^5\,\Omega$.

The wing tip displacement for the airflow speed of 10 m/s is presented in Figure 6(b). This displacement is obtained exactly at the tip half-chord point of the symmetric wing. As can be observed in the detailed view of Figure 6(b), after the initial transients, the oscillations decay at the short-circuit resonance frequency ($\omega_{sc} = 1.83\text{Hz}$) for a load resistance of $R_l = 10^2\,\Omega$. The oscillation frequency moves to the open-circuit value ($\omega_{oc} = 2.14\text{Hz}$) as the value of load resistance is increased to $R_l = 10^6\,\Omega$. The resistive shunt damping effect of piezoelectric power generation is observed in

Table 1. Material and electromechanical properties of PZT-5A.

Mass density (kg/m^3)	7800
Dielectric constant, K_3^T	1800
c_{11}^E, c_{22}^E (GPa)	120.3
c_{12}^E (GPa)	75.2
c_{13}^E, c_{23}^E (GPa)	75.1
c_{33}^E (GPa)	110.9
c_{66}^E (GPa)	22.7
e_{31}, e_{32} (C/m^2)	−5.2
e_{33} (C/m^2)	15.9

Table 2. Geometric and material properties of the wing.

Length of the wing (mm)	1200
Width of the wing (mm)	240
Thickness of the wing (mm)	3
Young's modulus of the wing (GPa)	70.0
Mass density of the substructure (kg/m^3)	2750
Proportionality constant – α (rad/s)	0.1635
Proportionality constant – β (s/rad)	4.1711×10^{-4}

Figure 6(b). The amplitude of tip motion is not modified considerably when the value of load resistance is increased from $R_l = 10^2\,\Omega$ to $10^4\,\Omega$. The maximum shunt damping effect is observed for the value of load resistance $R_l = 10^5\,\Omega$, the optimal one among the sample resistance values tested in this case.

In the second piezoaeroelastic case of this work the airflow speed is increased to 30 m/s. As mentioned previously, the maximum aerodynamic damping is around this airflow speed (Figure 5). As a result, any oscillation due to flow excitation is rapidly damped out (Figure 7(b)) reducing the amount of the electrical energy converted from vibrations. According to Figure 7(a), almost no power output is obtained after 0.5 s for this condition as the oscillations decay rapidly. The peak power output at this airspeed is two orders of magnitude larger than the power harvested for the airflow speed of 10 m/s. Therefore, although the total damping on the structure (Figure 5) is larger for the 30 m/s case, larger aerodynamic forces result in a larger peak power.

The time history of power output at the short-circuit flutter speed (40 m/s) for the continuous-electrode case is shown in Figure 8(a). The power output increases as the value of load resistance is increased from $R_l = 10^2\,\Omega$ to $10^4\,\Omega$ (Figure 8(a)). Clearly the value of the load resistance $R_l = 10^4\,\Omega$ provides the maximum power output among the set of load resistance values considered here. Note that the time history of the largest power output case exhibits a decaying behavior which is due to the strong shunt damping effect of power generation, which can also be verified in the vibration response given by Figure 8(b). If R_l is increased to $R_l = 10^5\,\Omega$, the power output decreases. When the load resistance is further increased to $R_l = 10^6\,\Omega$ (close to open-circuit condition) the power output is considerably reduced to values similar to the ones obtained close to short-circuit conditions with $R_l = 10^2\,\Omega$ (enlarged view in Figure 8(a)).

The time history of power output for the segmented-electrode case at the short-circuit flutter speed of the continuous-electrode case ($V = 40$ m/s) is shown in

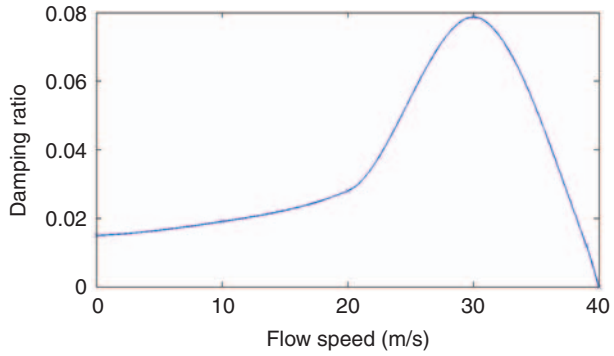

Figure 5. *Variation of the total (structural and aerodynamic) damping of the second vibration mode with increasing flow speed.*

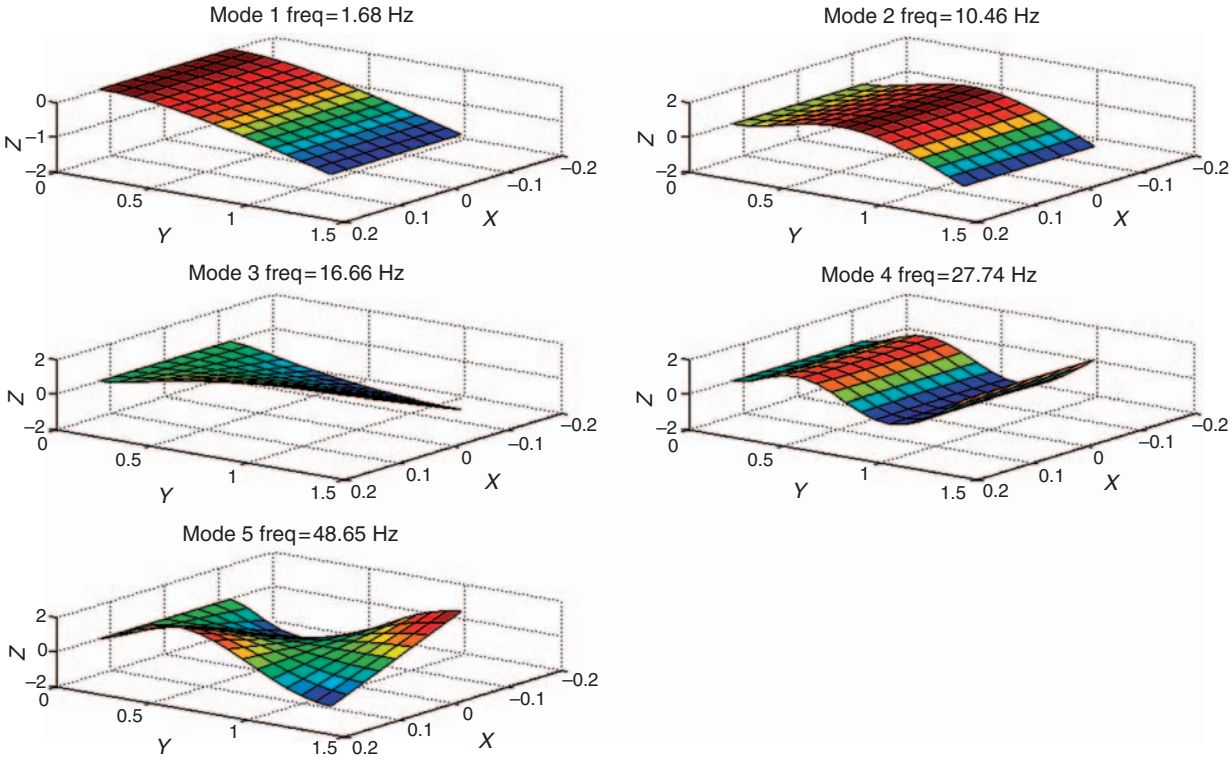

Figure 4. *The mode sequence and the undamped natural frequencies of the plate-like wing obtained from the FE model for short-circuit conditions.*

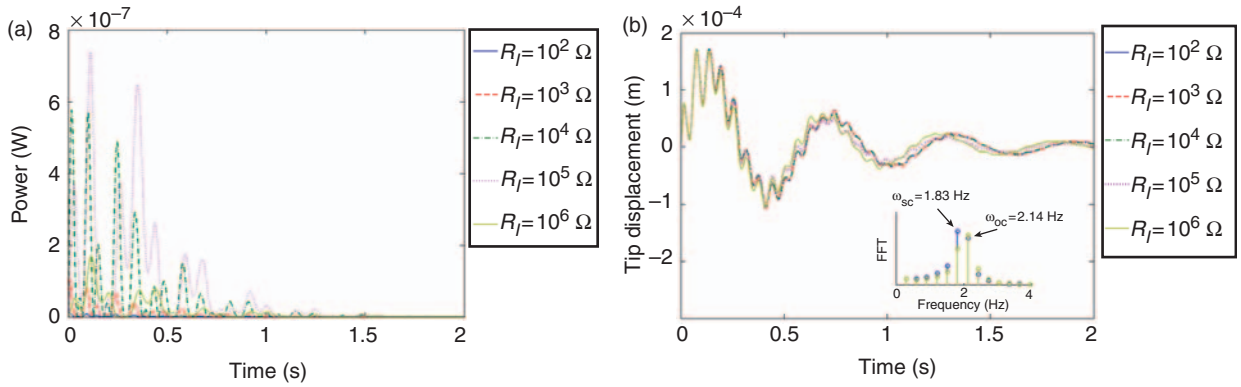

Figure 6. *(a) Power output and (b) tip displacement for five different values of load resistance at an airflow speed of 10 m/s.*

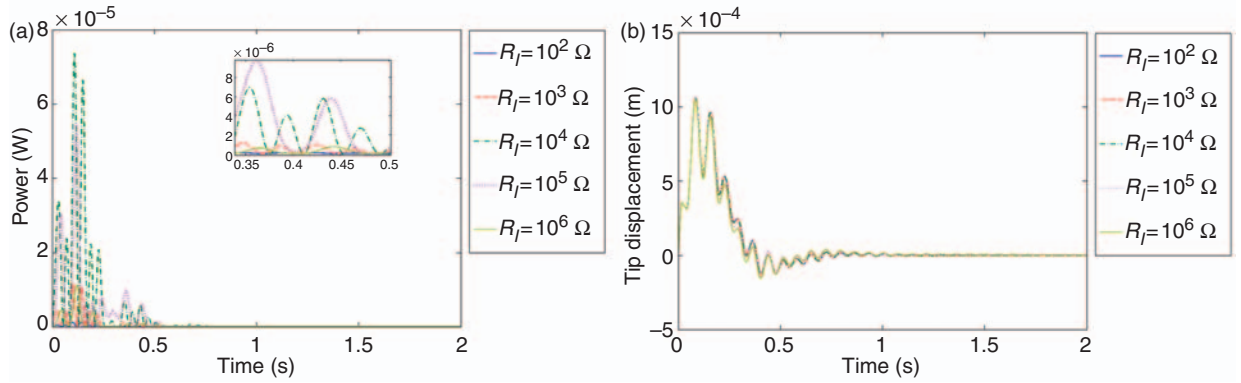

Figure 7. *(a) Power output and (b) tip displacement for five different values of load resistance at an airflow speed of 30 m/s.*

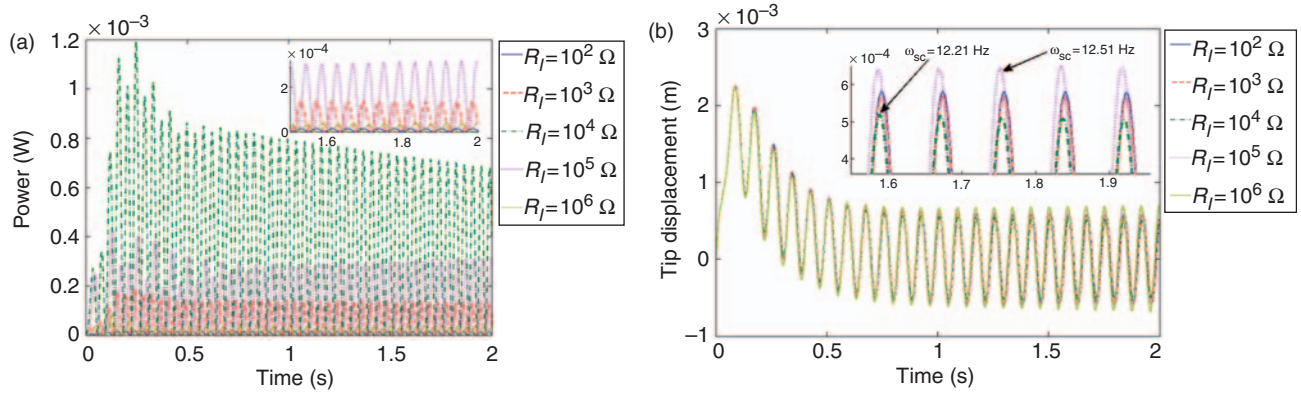

Figure 8. *(a) Power output and (b) tip displacement histories for the continuous-electrode configuration (five different values of load resistance at the short-circuit flutter speed of the continuous-electrode configuration).*

Figure 9(a). The power output increases as the load resistance is increased from the short-circuit conditions to $R_l = 10^4\,\Omega$, which is given in Figure 9(a). If R_l is increased to $10^5\,\Omega$ and $10^6\,\Omega$, the amplitude of power output decreases. As in the continuous-electrode case, the value of load resistance $R_l = 10^4\,\Omega$ provides the maximum power output among the set of load resistance values considered here. It is important to note that the peak power obtained for the segmented-electrode case is larger than the peak power obtained for the continuous-electrode case (for all values of load resistance). Cancelation of the electrical output of the torsional

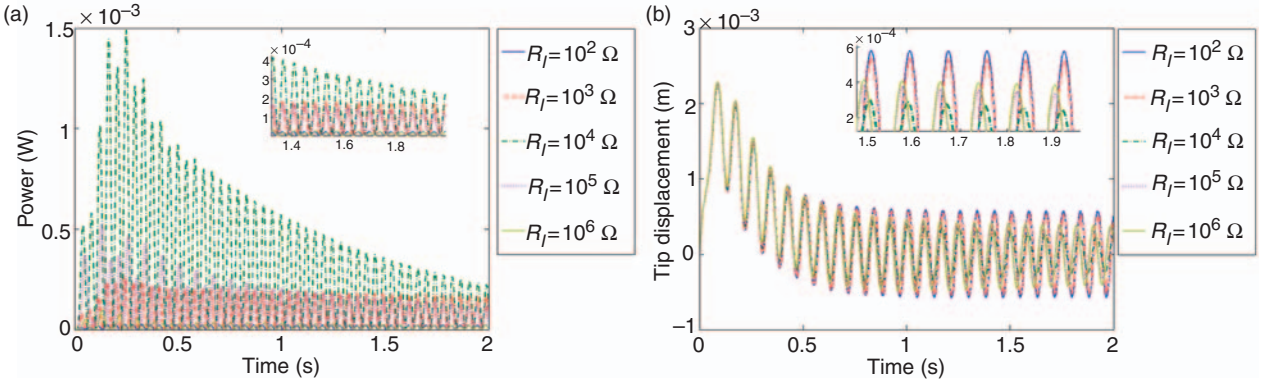

Figure 9. *(a) Power output and (b) tip displacement histories for the segmented-electrode configuration (five different values of load resistance at the short-circuit flutter speed of the continuous-electrode configuration).*

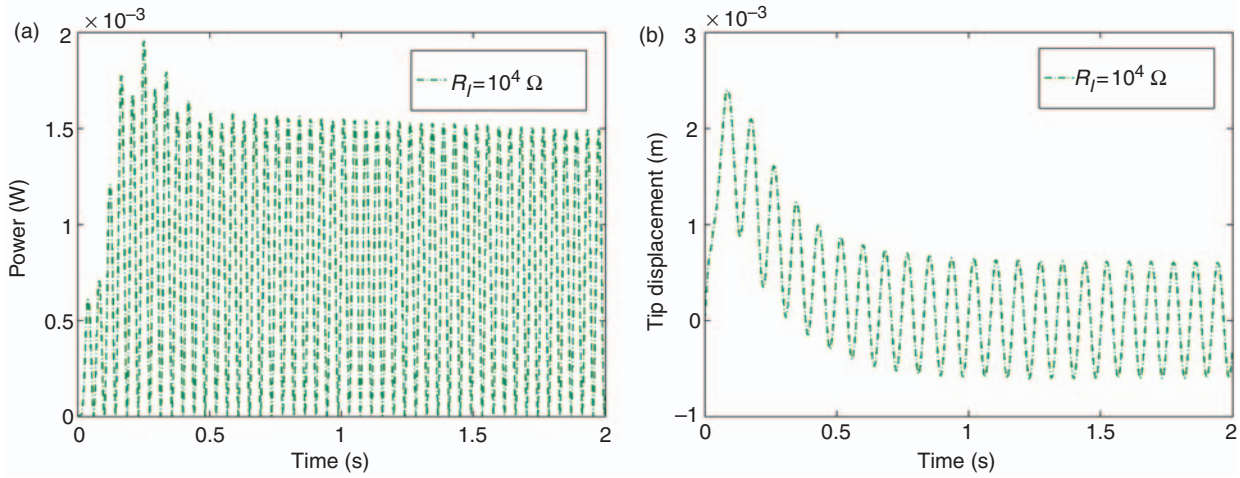

Figure 10. *(a) Power output and (b) tip displacement histories for the segmented-electrode configuration at 41 m/s* ($R_l = 10^4\ \Omega$).

modes is avoided with segmented electrodes. Recall from Figure 8(a) that the decaying behavior (due to the shunt damping effect of power generation) is observed only for the optimum load resistance ($R_l = 10^4\,\Omega$) in the continuous-electrode case. If R_l is increased to $10^5\,\Omega$, the generator wing becomes even unstable. However the response history of the wing with segmented electrodes shows a decaying behavior for any load resistance considered here as depicted in Figure 9(a) and (b). For $R_l = 10^4\,\Omega$, the vibration attenuation becomes even more evident as the time proceeds. In general, torsional modes are excited during the coupled flutter motions. Therefore the shunt damping effect can be improved by using segmented electrodes in piezoaeroelastic problems.

The time history of power output for the segmented electrodes case at 41 m/s and $R_l = 10^4\,\Omega$ is shown in Figure 10(a). Although the modification of the flutter characteristics is not the main motivation here, one can observe at this airflow speed the typical flutter behavior with a persistent vibration response (Figure 10(b)). Therefore, one can define 41 m/s as the flutter speed of the segmented-electrode case for $R_l = 10^4\,\Omega$. The power output is continuously extracted over the time and the peak power observed in Figure 10(a) is larger than that of the previous cases (continuous and segmented electrodes at 40 m/s) when the optimum load resistance (among the ones tested here) is used.

SUMMARY AND CONCLUSIONS

In this article, piezoaeroelastic modeling of a generator wing with embedded piezoceramics is presented for continuous- and segmented-electrode configurations. The piezoaeroelastic model is obtained by combining an electromechanically coupled FE model based on the classical plate theory with an unsteady vortex-lattice model. A resistive electrical load is considered in the electrical domain. The resulting equations governing the coupled system dynamics are solved simultaneously by addressing the dependence of the aerodynamic loads to the structural motion and vice versa.

The conversion of aeroelastic vibrations into electrical energy has been investigated at several airflow speeds for a set of resistors considered in this work. The aeroelastic analysis depends on the variation of aerodynamic damping with increasing airflow speed. Low aerodynamic damping is obtained at low airspeeds and close to the flutter speed. However, reduced deformations are obtained due to the low aerodynamic loads at lower airflow speeds. The most favorable condition for power harvesting occurs for airflow speeds higher than 30 m/s (for the case study covered here) and especially close to flutter condition (which is the other extreme condition of low aerodynamic damping). In these cases, the aerodynamic loads are obviously larger than those in the previously described cases. At the flutter speed, the aerodynamic damping vanishes and the oscillations are persistent. Although this condition is avoided in a real aircraft, it is the best condition as a concept demonstration for the generator wing investigated here using the linear piezoaeroelastic model.

The effect of segmented electrodes on the piezoaeroelastic response of a cantilevered thin plate (representing the generator wing) with embedded piezoceramics is investigated around 40 m/s (the short-circuit flutter speed) for a set of electrical load resistance. The peak power generated for the segmented-electrode case is larger than that generated for the continuous-electrode case for any value of load resistance considered here at 40 m/s. Cancelation of the electrical output of torsional motions is avoided by using segmented electrodes. Therefore, in addition to the benefit of using segmented electrodes in electrical power generation, it is shown that the resistive shunt damping effect can also be improved using segmented electrodes in piezoaeroelastic problems. The decaying behavior due to the shunt damping effect of power generation is observed for any value of load resistance in the segmented electrode case. For the continuous-electrode case, however, the neutral stability of the wing at the short-circuit flutter speed (40 m/s) is converted to a stable response only for the optimum load resistance ($R_l = 10^4\,\Omega$). Therefore, the modified flutter condition of the segmented-electrode case is obtained at the airflow speed of 41 m/s for $R_l = 10^4\,\Omega$. For this last case, the power output is continuously extracted and the peak power is also larger than the previous cases discussed here.

ACKNOWLEDGEMENTS

The authors gratefully acknowledge the support of the Air Force Office of Scientific Research under the grants F 9550-06-1-0326 'Energy Harvesting and Storage Systems for Future Air Force Vehicles' and F 9550-09-1-0625 'Simultaneous Vibration Suppression and Energy Harvesting' monitored by Dr. B. L. Lee. The authors also gratefully acknowledge the support of CAPES and also gratefully acknowledge CNPq and FAPEMIG for partially funding the present research work through the INCT-EIE.

REFERENCES

Agneni, A., Del Sorbo, M., Mastroddi, F. and Polli, G.M. 2006. "Multi-modal Damping by Shunted Piezo-patches: Possible Aeroelastic Applications," *International Journal of Applied Electromagnetics and Mechanics*, 24:1–24.

Agneni, A., Mastroddi, F. and Polli, G.M. 2003. "Shunted Piezoelectric Patches in Elastic and Aeroelastic Vibrations," *Computers and Structures*, 81:91–105.

Anton, S.R. and Inman, D.J. 2008. "Vibration Energy Harvesting for Unmanned Air Vehicles," *Smart Structures and Materials 2008: Active and Passive Smart Structures and Integrated Systems II*; *Proc. SPIE* 6928, San Diego.

Anton, S.R. and Sodano, H.A. 2007. "A Review of Power Harvesting Using Piezoelectric Materials 2003–2006," *Smart Materials and Structures*, 16:R1–R21.

Beeby, S.P., Tudor, M.J. and White, N.M. 2006. "Energy Harvesting Vibration Sources for Microsystems Applications," *Measurement Science and Technology*, 13:R175–R195.

Benini, G.R., Belo, E.M. and Marques, F.D. 2004. "Numerical Model for the Simulation of Fixed Wings Aeroelastic Response," *Journal of the Brazilian Society of Mechanical Sciences & Engineering*, 26:129–136.

Bilgen, O., Kochersberger, K., Diggs, E., Kurdila, A. and Inman, D. J. 2007. "Morphing Wing Micro-air-vehicles via Macro-fiber-composite Actuators," In: *48th AIAA/ASME/ASCE/AHS/ASC Structures, Structural Dynamics, and Materials Conference*, Honolulu, Hawaii.

Brown, E.L. 2003. "Integrated Strain Actuation in Aircraft with Highly Flexible Composite Wings," PhD Dissertation, Department of Mechanical Engineering (MIT).

Cesnik, C.E.S. and Ortega-Morales, M. 2001. "Active Aeroelastic Tailoring of Slender Flexible Wings," In: *International Forum on Aeroelasticity and Structural Dynamics*, Madrid, Spain.

Cesnik, C.E.S. and Shin, S.-J. 2001. "On the Modeling of Active Helicopter Blades," *International Journal of Solids and Structures*, 38:1765–1789.

Cook-Chennault, K.A., Thambi, N. and Sastry, A.M. 2008. "Powering MEMS Portable Devices – a Review of Non-regenerative and Regenerative Power Supply Systems with Emphasis on Piezoelectric Energy Harvesting Systems," *Smart Materials and Structures*, 17:043001.

De Marqui Jr, C., Erturk, A. and Inman, D.J. 2009a. "An Electromechanical Finite Element Model for Piezoelectric Energy Harvester Plates," *Journal of Sound and Vibration*, 327:9–25.

De Marqui Jr, C., Erturk, A. and Inman, D.J. 2009b. "Finite Element Analysis of a UAV Wing Spar with Piezoceramics for Vibration Energy Harvesting," In: *50th AIAA/ASME/ASCE/AHS/ASC Structures, Structural Dynamics, and Materials Conference*, Palm Springs, CA.

Elvin, N.G. and Elvin, A.A. 2009. "A Coupled Finite Element – Circuit Simulation Model for Analyzing Piezoelectric Energy Generators," *Journal of Intelligent Material Systems and Structures*, 20:587–595.

Erturk, A. and Inman, D.J. 2008a. "Issues in Mathematical Modeling of Piezoelectric Energy Harvesters," *Smart Materials and Structures*, 17:065016 (14pp).

Erturk, A. and Inman, D.J. 2008b. "A Distributed Parameter Electromechanical Model for Cantilevered Piezoelectric Energy Harvesters," *ASME Journal of Vibration and Acoustics*, 130:041002.

Erturk, A. and Inman, D.J. 2009. "An Experimentally Validated Bimorph Cantilever Model for Piezoelectric Energy Harvesting from Base Excitations," *Smart Materials and Structures*, 18:025009 (18pp).

Erturk, A., Renno, J.M. and Inman, D.J. 2009a. "Modeling of Piezoelectric Energy Harvesting from an L-shaped Beam-mass Structure with an Application to UAVs," *Journal of Intelligent Material Systems and Structures*, 20:529–544.

Erturk, A., Tarazaga, P., Farmer, J.R. and Inman, D.J. 2009b. "Effect of Strain Nodes and Electrode Configuration on Piezoelectric Energy Harvesting from Cantilevered Beams," *ASME Journal of Vibration and Acoustics*, 131:011010.

Friedmann, P.P. 1998. "Rotary-wing Aeroelastic Scaling and its Application to Adaptive Materials Based Actuation," In: *39th AIAA/ASME/ASCE/AHS/ASC Structures, Structural Dynamics, and Materials Conference and Exhibit, and AIAA/ASME/AHS Adaptive Structures Forum*, Long Beach, CA.

Harder, R.L. and Desmarais, R.N. 1972. "Interpolation using Surface Splines," *Journal of Aircraft*, 9:189–191.

http://www.efunda.com/materials/piezo/material_data (Accessed December 2009).

Katz, J. and Plotkin, A. 2001. *Low Speed Aerodynamics*, Cambridge University Press, Cambridge.

Kim, S., Clark, W.W. and Wang, Q.M. 2005a. "Piezoelectric Energy Harvesting with a Clamped Circular Plate: Analysis," *Journal of Intelligent Material Systems and Structures*, 16:847–854.

Kim, S., Clark, W.W. and Wang, Q.M. 2005b. "Piezoelectric Energy Harvesting With a Clamped Circular Plate: Experimental Study," *Journal of Intelligent Material Systems and Structures*, 16:855–863.

Lambert, J.D. 1991. *Numerical Methods for Ordinary Differential Systems: The Initial Value Problem*, Wiley, Chichester.

Lazarus, K.B., Crawley, E.F. and Lin, C.Y. 1995. "Fundamental Mechanism of Aeroelastic Control with Control Surface and Strain Actuation," *Journal of Guidance, Control and Dynamics*, 18:10–17.

Librescu, L. and Na, S. 2000. "Vibration and Dynamic Response Control of Elastically Tailored Nonuniform Adaptive Aircraft Wings," *41st AIAA/ASME/ASCE/AHS/ASC Structures, Structural Dynamics, and Material Conference and Exhibit*, Atlanta, GA.

Magoteaux, K.C., Sanders, B. and Sodano, H.A. 2008. "Investigation of Energy Harvesting Small Unmanned Air Vehicle," In: *Smart Structures and Materials 2008: Active and Passive Smart Structures and Integrated Systems II Proc. SPIE* 6928, San Diego.

McGowan, A.R., Heeg, J. and Lake, R. 1996. "Results of Wind-tunnel Testing from the Piezoelectric Aeroelastic Tailoring Investigation," In: *37th AIAA/ASCE/AHS/ASC Structures, Structural Dynamics and Materials Conference*, Salt Lake City, UT.

Pines, D.J. and Bohorquez, F. 2006. "Challenges Facing Future Micro-Air-Vehicle Development," *Journal of Aircraft*, 43:290–305.

Priya, S. 2007. "Advances in Energy Harvesting using Low Profile Piezoelectric Transducers," *Journal of Electroceramics*, 19:167–184.

Rupp, C.J., Evgrafov, A., Maute, K. and Dunn, M.L. 2009. "Design of Piezoelectric Energy Harvesting Systems: A Topology Optimization Approach Based on Multilayer Plates and Shells," *Journal of Intelligent Material Systems and Structures*, 20:1923–1939.

Schultz, M.R. and Hyer, M.W. 2004. "A Morphing Concept based on Unsymmetric Composite Laminates and Piezoceramic MFC Actuators," In: *45th AIAA/ASME/ASCE/AHS/ASC Structures, Structural Dynamics & Materials Conference*, Palm Springs, CA.

Sheta, E.F., Moses, R.W., Huttsell, L.J. and Harrand, V.J. 2003. "Active Control of F/A-18 Vertical Tail Buffeting using Piezoelectric Actuators," In: *44th AIAA/ASME/ASCE/AHS Structures, Structural Dynamics, and Materials Conference*, Norfolk, VA.

Sodano, H.A., Inman, D.J. and Park, G. 2004. "A Review of Power Harvesting from Vibration Using Piezoelectric Materials," *The Shock and Vibration Digest*, 36:197–205.

Wickramasinghe, V.K., Chen, Y. and Zimcik, D.G. 2007. "Experimental Evaluation of an Advanced Buffet Suppression System on Full-scale F/A-18 Fin," *Journal of Aircraft*, 44:733–740.

Yang, Y. and Tang, L. 2009. "Equivalent Circuit Modeling of Piezoelectric Energy Harvesters," *Journal of Intelligent Material Systems and Structures*, 20:2223–2235.